Available online at www.sciencedirect.com
SCIENCE DIRECT®
International Journal of Heat and Mass Transfer 47 (2004) 3617–3629
International Journal of HEAT and MASS TRANSFER
www.elsevier.com/locate/ijhmt

Three-dimensional simulation of chemically reacting gas flows in the porous support structure of an integrated-planar solid oxide fuel cell

B.A. Haberman *, J.B. Young

Hopkinson Laboratory, Cambridge University Engineering Department, Cambridge CB2 1PZ, UK

Received 26 November 2003; received in revised form 28 April 2004

Abstract

The behaviour of an integrated-planar solid oxide fuel cell (IP-SOFC) strongly depends on the reactive diffusive flows within its porous support structure. Fuel is transported through the porous structure to the anodes of the electrochemical cells and the structure may be impregnated with the required catalysts for the steam reforming of methane. It is important to be able to calculate the distribution of gas properties within the porous structure in order to predict the performance of each cell and to determine the amount of internal reforming that takes place. This paper describes a three-dimensional numerical calculation method which has been developed to solve the governing equations in the porous structure. The calculation method includes the interaction between the flow in the porous medium and that in the adjacent fuel supply channel. The results highlight the importance of the kinetics of the reforming reaction and the thermal boundary conditions, both of which have a significant effect on the flow field within the porous structure.

Keywords: SOFC; Porous; Simulation; Chemical reaction

1. Introduction

The solid oxide fuel cell (SOFC) is widely expected to play a major rôle in the medium-sized electricity power generation industry (1–10 MW) in the coming decades. The benefits include the possibility of operation using natural gas, zero emissions of nitrogen and sulphur oxides, and very high cycle efficiencies when combined with a gas turbine. All present types of SOFC reform their fuels to hydrogen, either externally or internally, and hence longer term attractions include flexibility in fuel choice and the possibility of CO_2 capture by the use of a suitable fuel pre-processing technique.

Three configurations of SOFC are currently under development in industry: the planar, tubular, and integrated-planar designs. The planar SOFC can have sealing problems caused by thermal expansion. The tubular SOFC is superior in this respect but manufacturing costs are currently very high. The integrated-planar SOFC (IP-SOFC), pioneered by Rolls-Royce [1], see Fig. 1, combines the advantages of the planar and tubular designs without the thermal–mechanical disadvantages of the former or the fabrication costs of the latter. Its potential is currently creating great interest in the fuel cell community.

The electrochemical cells of an IP-SOFC are supported on a thick porous ceramic layer adjacent to the anode and Fig. 2 shows the flow of gases and ions within the structure. O_2 gas diffuses through the cathode and the electrochemical reaction,

$$\frac{1}{2}O_2 + 2e^- \rightarrow O^{2-} \tag{1}$$

* Corresponding author.
E-mail addresses: b.haberman.01@cantab.net (B.A. Haberman), jby@eng.cam.ac.uk (J.B. Young).

0017-9310/$ - see front matter © 2004 Elsevier Ltd. All rights reserved.
doi:10.1016/j.ijheatmasstransfer.2004.04.010

Nomenclature

D_{ij}	binary diffusion coefficient
d_p	mean pore size
e	specific energy
g	mass flux vector
h	specific enthalpy
K	permeability (m^2)
K_p	equilibrium constant
L	porous domain dimension
M	molar mass
n	number of species
p	pressure
q	heat flux vector
R	molar gas constant
S	mass rate of production per unit volume
s	surface area vector
t	time
T	temperature
U	velocity vector
V	volume
X	mole fraction
Y	mass fraction

Greeks symbols

β	tortuosity
ε	porosity
λ	thermal conductivity
μ	dynamic viscosity
ρ	density

Subscripts

g	gas mixture
i, j	component species
p	pore
s	solid
0	fuel channel inlet

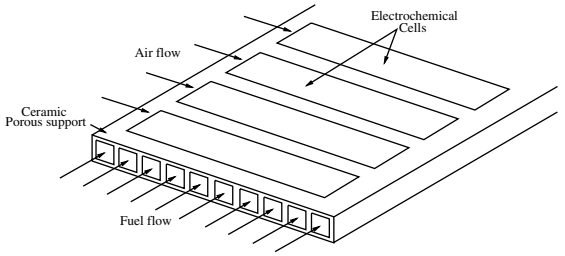

Fig. 1. The Rolls-Royce IP-SOFC. Schematic diagram of a module. The electrochemical cells are printed on both sides of the ceramic structure.

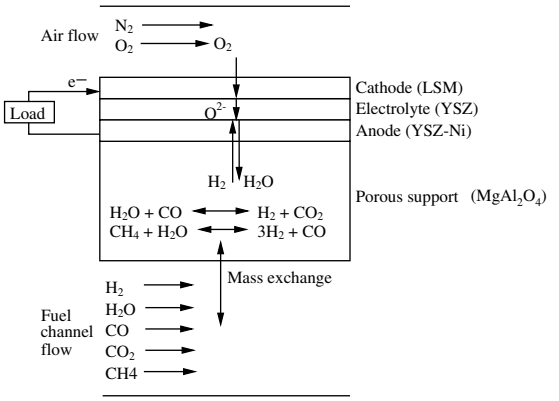

Fig. 2. Gas and ion transport and chemical reactions in an IP-SOFC.

occurs at, or near, the cathode–electrolyte interface. The O^{2-} ions migrate across the electrolyte while H_2 gas diffuses through the porous support and anode layers. The electrochemical reactions,

$$H_2 \rightarrow 2H^+ + 2e^- \tag{2}$$

$$2H^+ + O^{2-} \rightarrow H_2O \tag{3}$$

occur at, or near, the anode–electrolyte interface and the reaction product H_2O diffuses back into the fuel channel. The porous support layer controls the convection and diffusion of gases to and from the anode. The performance of each electrochemical cell is intrinsically linked to the gas composition and temperature at the anode surfaces.

If the fuel supply is a reformate mixture of natural gas, then CH_4, CO and CO_2 will also be present and it is necessary to consider the water–gas shift and methane reforming reactions,

$$H_2O + CO \leftrightarrow H_2 + CO_2 \quad \Delta H_{298} = -41.1\ \mathrm{kJ\,mol^{-1}} \tag{4}$$

$$CH_4 + H_2O \leftrightarrow 3H_2 + CO \quad \Delta H_{298} = 206\ \mathrm{kJ\,mol^{-1}} \tag{5}$$

which occur in (and may be catalysed by) the porous support material. In this study, it is assumed that the electrochemical conversion rate of CO is negligible compared to that of H_2.

There have been a number of studies focusing on the flow conditions and gas concentration distribution within the porous structure of a planar SOFC [2,3]. Thus, Lehnert et al. [2] modelled the multi-component mass and momentum equations in an isothermal analysis of the reactive flows and determined the variation of gas composition and reaction rate through the thickness

of the porous structure. In reality, of course, the chemical reaction rates are strongly temperature dependent and, as shown by Ackmann et al. [3], it is important to include the energy equation as well as the momentum and species conservation equations.

The studies [2,3] used fixed boundary conditions at the interface between the porous structure and the fuel channel, see Fig. 2. In practice, in an IP-SOFC the mass and enthalpy exchange between the fuel flowing in this channel and the porous support will result in variable conditions at the interface. Yuan et al. [4] included this interaction in their three-dimensional analysis but they took no account of chemical reactions.

This paper is concerned with the three-dimensional numerical simulation of the multi-component reactive gas flows in the porous support structure of an IP-SOFC. The calculation procedure models thermal effects in the gas and solid, and includes the effect of the interaction with the adjacent fuel channel.

2. The physical model

2.1. General description

Fig. 1 shows the layout of one end of an IP-SOFC module as developed at Rolls-Royce. A full size module has up to 20 cells printed on the top and bottom surfaces. For illustrative purposes however, it is assumed that the module is very much shorter and has only five cells. The computational domain, shown in Fig. 3, is the porous support structure directly above the central fuel gas channel. It extends along the top of the channel for the entire length of the module and has five cells printed transversely across its top surface. The cells are omitted from Fig. 3 for clarity.

The overall thickness of the electrochemical layers is only about 100 μm. The computational domain has the dimensions $L_x = 100$ mm, $L_y = 1$ mm, $L_z = 2$ mm and and is in direct contact with the anode layer of the cells.

2.2. Boundary conditions

For this investigation the boundary conditions associated with the electrochemical reactions at the

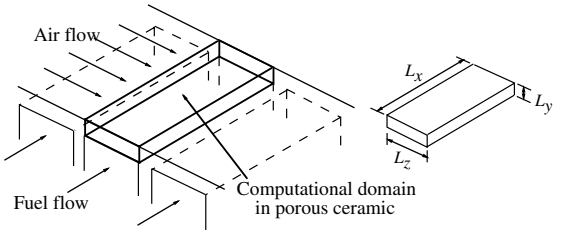

Fig. 3. Detail of the computational domain.

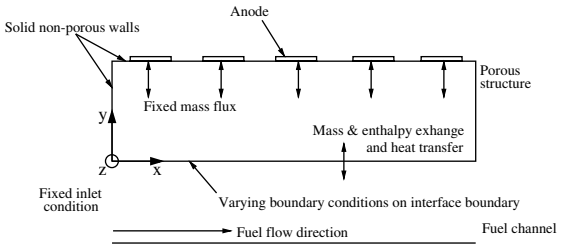

Fig. 4. Cross-section through the computational domain.

anode/electrolyte interface are applied directly to the top surface of the porous structure. This is considered a reasonable assumption as the anode is very thin (50 μm) relative to the porous structure (1 mm). Fig. 4 shows a cross-section along the length of the computational domain and the boundary conditions visible in this projection. The coordinate system shown in Fig. 4 is used throughout this paper.

It is assumed that the domain has adiabatic solid (non-porous) wall boundary conditions on its $z = 0$ and $z = L_z$ faces which are in contact with identical porous regions. The $x = L_x$ face and parts of the $y = L_y$ face not directly underneath a cell are also treated as solid adiabatic walls. The $x = 0$ face, adjacent to the channel inlet, is treated as a solid wall with a fixed temperature. The $y = 0$ face is the interface boundary between the porous structure and the flow in the fuel channel. The gas composition and temperature along the fuel channel vary due to the mass and enthalpy transfer to the porous structure. An inlet boundary condition at $x = 0$ and a channel half-width y_c are also specified for the fuel channel.

It is assumed that the electric current density in each cell is uniform at 300 mA cm^{-2}. The corresponding rates of steam production and hydrogen consumption at the anode/porous surface can then be deduced from Eqs. (2) and (3). The heat flux from the anode surface is arbitrarily set to 250 Wm^{-2} to take account of the heat released during the electrochemical reaction at the anode/electrolyte interface. The gas composition fixed at the fuel channel inlet is 30% reformed methane fuel, see Table 1.

The heat and mass fluxes normal to the boundary surfaces (q_n, g_n) and the fuel channel inlet properties used for the simulation are all given in Table 2.

Table 1
Inlet fuel composition from Lehnert et al. [2]

$X_{H_2} = 0.263$
$X_{H_2O} = 0.493$
$X_{CO_2} = 0.044$
$X_{CO} = 0.029$
$X_{CH_4} = 0.171$

Table 2
Boundary conditions

Location	Boundary condition
$y = L_y$ face underneath a cell	$g_{y,\mathrm{CO}} = 0$
	$g_{y,\mathrm{H_2O}} = -0.280\ \mathrm{g\,s^{-1}\,m^{-2}}$
	$g_{y,\mathrm{H_2}} = 0.032\ \mathrm{g\,s^{-1}\,m^{-2}}$
	$g_{y,\mathrm{CO_2}} = 0$
	$g_{y,\mathrm{CH_4}} = 0$
	$q_y = -250\ \mathrm{W\,m^{-2}}$
Fuel gas channel inlet	$p_0 = 100$ kPa
	$T_0 = 1123$ K
	$X_{\mathrm{CH_4},0} = 0.171$
	$X_{\mathrm{CO},0} = 0.029$
	$X_{\mathrm{H_2O},0} = 0.493$
	$X_{\mathrm{H_2},0} = 0.263$
	$X_{\mathrm{CO_2},0} = 0.044$
	$\dot{m}_0 = 2 \times 10^{-4}\ \mathrm{g\,s^{-1}}$
	$y_c = 1.5$ mm
$x = L_x$ $z = 0, L_z$ faces	$g_n = 0$
	$q_n = 0$
$x = 0$ face	$g_x = 0$
	$T = 1123$ K

Table 3
Properties of the ceramic porous material

Mean pore size	$d_p = 10\ \mu$m
Permeability	$K = 3.125 \times 10^{-12}\ \mathrm{m^2}$
Porosity	$\varepsilon = 0.5$
Density	$\rho_s = 2000\ \mathrm{kg\,m^{-3}}$
Thermal conductivity	$\lambda_s = 1.0\ \mathrm{W\,m^{-1}\,K^{-1}}$

2.3. Physical properties of the porous ceramic

The porous material is assumed to be $MgAL_2O_4$, a ceramic often used as a support for catalysts. The ceramic is assumed to be isotropic with the properties given in Table 3. It should be noted that the pore size is significantly larger than the mean free path of the gas molecules and so diffusion can be modelled using continuum theory.

3. The governing equations

3.1. The momentum equation for the flow in the porous structure

The performance of porous materials in building insulation and in hydrology has been investigated extensively. The starting point for analysis is the empirical Darcy equation which describes the balance between the force from the pressure gradient ∇p and the frictional resistance from the solid material,

$$-\nabla p = \frac{\mu_g \varepsilon}{K}\mathbf{U}_p \tag{6}$$

where $\mathbf{U}_p$ is the pore velocity vector, ε is the porosity (the volume fraction of void space), μ_g is the dynamic viscosity of the gas mixture and K is the permeability. The volume flow rate per unit area through the porous structure is obtained by multiplying $\mathbf{U}_p$, the mean velocity within a pore, by ε. K was originally experimentally determined by Darcy but can be estimated from the mean pore diameter d_p. The pore Reynolds number is defined by

$$Re_p = \frac{\rho_g |\mathbf{U}_p| d_p}{\mu_g} \tag{7}$$

where ρ_g is the gas mixture density. Eq. (6) is valid for $Re_p < 1$ [5], when pressure loss is dominated by pore friction and the inertia terms usually present in a momentum equation are insignificant. In the present application, the maximum value of Re_p is about 0.0001 and hence the use of Eq. (6) is well justified.

The Darcy equation describes the flow in the porous structure well away from the walls. It cannot model a no-slip condition at a wall nor the resulting boundary layers. With reference to Fig. 4, it can be seen that boundary layers may develop along the solid walls bounding the $x = 0$, $x = L_x$ and $y = L_y$ faces of the computational domain, and also at the $y = 0$ face where the porous structure interfaces with the fuel channel. In the Appendix A, an approximate theoretical analysis is presented in order to estimate the likely magnitudes of these boundary layers. It is found that, although the boundary layer thicknesses are typically only about 1–3% of the ceramic support thickness, Eq. (6) can be modified to allow their calculation. This is done by adding the so-called 'Brinkman' term [6–8] to the Darcy equation which then becomes

$$-\nabla p = \frac{\varepsilon \mu_g}{K}\mathbf{U}_p - \nabla \cdot (\mu_g \nabla)\mathbf{U}_p \tag{8}$$

where the normal stresses in the final term are, as usual, ignored.

3.2. Conservation of species

A conservation equation can be written for each of the n individual species,

$$\frac{\partial \rho_i}{\partial t} + \nabla \cdot (\rho_i \mathbf{U}_{pi}) = S_i \tag{9}$$

where ρ_i is the density, $\mathbf{U}_{pi}$ is the pore velocity vector and S_i is the rate of production per unit volume due to chemical reaction, all of species i. The flux vector of the ith species $\rho_i \mathbf{U}_{pi}$ is the sum of the convection and diffusion fluxes,

$$\rho_i \mathbf{U}_{pi} = \rho_i \mathbf{U}_p + \frac{\mathbf{g}_i}{\beta} \tag{10}$$

where the mass-averaged pore velocity $\mathbf{U}_p$ is the velocity calculated from the Darcy Equation (6), $\mathbf{g}_i$ is the diffusion mass flux relative to the mass-averaged velocity and β is the tortuosity. The diffusion mass fluxes can be derived from the Stefan–Maxwell relations

$$\nabla X_i = \frac{\widetilde{M}}{\rho_g} \sum_{j=1}^{n} \left(\frac{\mathbf{g}_j X_i}{M_j D_{ij}} - \frac{\mathbf{g}_i X_j}{M_i D_{ji}} \right) \tag{11}$$

where M_i is the molar mass of species i, $D_{ij} = D_{ji}$ is the binary diffusion coefficient of a mixture of the species i and j and $\widetilde{M}$ is the mean molar mass.

The Stefan–Maxwell relations can be written in matrix form for the first $n-1$ fluxes

$$(\nabla X) = -\frac{\widetilde{M}}{\rho_g}[B](\mathbf{g}) \tag{12}$$

where (∇X) and $(\mathbf{g})$ are matrices of size $(n-1)\times 3$ whose elements are the species mole fraction gradients and diffusion fluxes respectively. The matrix $[B]$ is a square matrix of order $n-1$ with components:

$$B_{ii} = \frac{X_i}{M_n D_{in}} + \frac{1}{M_i} \sum_{j=1, j\neq i}^{n} \frac{X_j}{D_{ij}} \tag{13}$$

$$B_{ij} = -X_i \left(\frac{1}{M_j D_{ij}} - \frac{1}{M_n D_{in}} \right) \tag{14}$$

The first $(n-1)$ diffusion fluxes are determined by inverting the matrix $[B]$. The nth flux $\mathbf{g}_n$ is then found from the condition that the diffusion fluxes sum to zero,

$$\mathbf{g}_n = -\sum_{j=1}^{n-1} \mathbf{g}_j \tag{15}$$

The non-reactive isothermal multi-component diffusion through the thickness of the porous support can be solved analytically if it is assumed that the flow is one-dimensional [9]. Fig. 5 shows a comparison of the analytical and numerical solutions for this diffusion problem specified by the boundary conditions in Table 2. The fuel channel inlet boundary conditions are fixed on the interface boundary ($y = 0$) and the mass fluxes at the boundary $y = L_y$ are calculated for a rather unrealistic current density of 3000 mA cm^{-2}. This is to amplify the mole fraction variations for illustration and code validation purposes. At 300 mA cm^{-2} there is very little variation across the porous support.

3.3. Conservation of energy

The equation governing the conservation of energy in the porous structure is

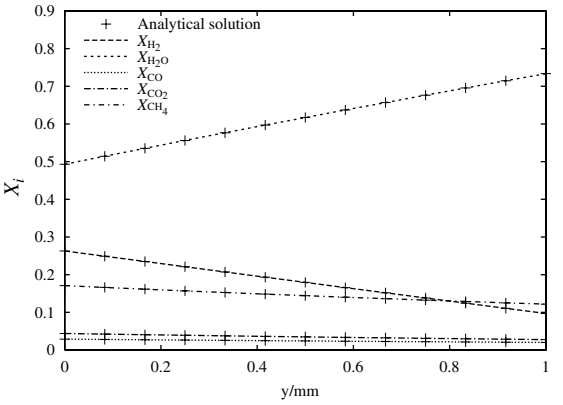

Fig. 5. Variation of mole fractions through the porous support assuming 1D non-reactive isothermal flow. The current density has been increased to 3000 mA cm^{-2} for illustration and code validation purposes.

$$\frac{\partial(\rho e)_{eff}}{\partial t} = -\nabla\cdot(\rho_g h_g \varepsilon \mathbf{U}_p) - \nabla\cdot\mathbf{q}_{eff} - \nabla\cdot\left(\sum_{i=1}^{n} \frac{\varepsilon \mathbf{g}_i}{\beta} h_i\right) \tag{16}$$

where h_g is the enthalpy of the gas mixture, $\mathbf{q}_{eff}$ is the heat conducted through both the solid and the gas and the final term on the right represents the enthalpy flux due to diffusion. h_i is the partial enthalpy of the ith species and is calculated from

$$h_i = h_{form,i} + \int_{T_0}^{T} c_{pi}(T')\mathrm{d}T' \tag{17}$$

where $h_{form,i}$ is the specific enthalpy of formation of species i at $T = T_0 = 298.15$ K. The specific enthalpy of the gas h_g is then given by

$$h_g = \sum_{i=1}^{n} Y_i h_i \tag{18}$$

where Y_i is the mass fraction of species i.

The total energy stored per unit volume of the porous structure $(\rho e)_{eff}$ is given by

$$(\rho e)_{eff} = \varepsilon \rho_g e_g + (1-\varepsilon)\rho_s e_s \tag{19}$$

where $(\rho e)_{eff}$ is a volume average of the energy stored per unit volume of gas $\rho_g e_g$ and the energy stored per unit volume of solid $\rho_s e_s$. e_g is given by

$$e_g = h_g - R_g T \tag{20}$$

where R_g is the specific gas constant for the mixture. The specific internal energy of the solid material e_s is given by

$$e_s = c_{ps}(T - T_0) + e_{s,298} \tag{21}$$

where c_{ps} is the specific heat capacity of the solid structure and $e_{s,298}$ is the specific internal energy at the datum temperature 298.15 K.

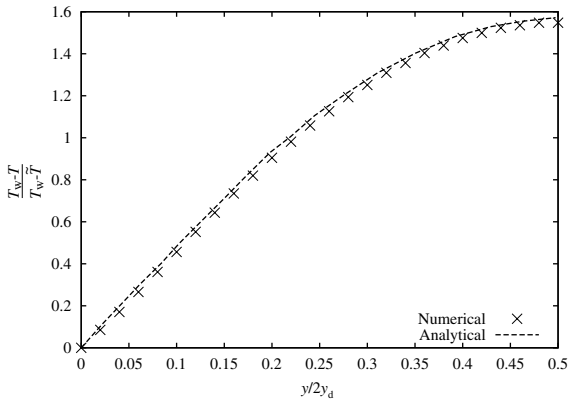

Fig. 6. Solution for the fully-developed thermal boundary layer in a porous channel bounded by isothermal walls. A comparison between the analytical solution of Kaviany [10] and the numerical solution using the method described in this paper.

The model assumes local thermal equilibrium between the gas and porous structure. The effective heat conduction flux, $\mathbf{q}_{\text{eff}}$, can therefore be defined in terms of the gradient of the common temperature T,

$$\mathbf{q}_{\text{eff}} = -(\varepsilon\lambda_{\text{g}} + (1-\varepsilon)\lambda_{\text{s}})\nabla T \tag{22}$$

where the thermal conductivities of the gas and solid are λ_{g} and λ_{s} respectively.

For code validation purposes, Fig. 6 shows a comparison between the analytical [10] and the numerical solution for the fully developed thermal boundary layer in a plane two-dimensional porous channel bounded by isothermal walls. The numerical solution was obtained by the method described in Section 4.

3.4. Reaction kinetics

The two chemical reactions under consideration are the water gas shift reaction

$$\text{H}_2\text{O} + \text{CO} \overset{k_{\text{sf}}}{\rightarrow} \text{H}_2 + \text{CO}_2 \tag{23}$$

and the methane reforming reaction,

$$\text{CH}_4 + \text{H}_2\text{O} \overset{k_{\text{rf}}}{\rightarrow} 3\text{H}_2 + \text{CO} \tag{24}$$

where k_{sf} and k_{rf} represent the forward catalysed reaction rate constants for the shift and reforming reactions respectively. The reverse reaction rate constants k_{sb} and k_{rb} can be determined from the equilibrium constants for the two reactions,

$$K_{ps} = \frac{k_{\text{sf}}}{k_{\text{sb}}} = \frac{p_{\text{H}_2}p_{\text{CO}_2}}{p_{\text{H}_2\text{O}}p_{\text{CO}}} = \frac{X_{\text{H}_2}X_{\text{CO}_2}}{X_{\text{H}_2\text{O}}X_{\text{CO}}} \tag{25}$$

$$K_{pr} = \frac{k_{\text{rf}}}{k_{\text{rb}}} = \frac{p_{\text{CO}}p_{\text{H}_2}^3}{p_{\text{CH}_4}p_{\text{H}_2\text{O}}} = \frac{X_{\text{CO}}X_{\text{H}_2}^3 p^2}{X_{\text{CH}_4}X_{\text{H}_2\text{O}}} \tag{26}$$

which are defined as functions of temperature by the following empirical equations given in [11],

$$K_{ps} = \exp(-0.2935Z^3 + 0.6351Z^2 + 4.1788Z + 0.3169) \tag{27}$$

$$K_{pr} = 1.0267\times 10^{10}\times\exp(-0.2513Z^4 + 0.3665Z^3 + 0.5810Z^2 - 27.134Z + 3.2770)\ (\text{Pa}^2) \tag{28}$$

$$Z = \frac{1000}{T(K)} - 1 \tag{29}$$

3.5. Rate constants

No rate data exists for the reactions catalysed by the porous material $MgAl_2O_4$. Data does exist, however, for the uncatalysed reactions [12–14] and also for the reactions catalysed by the anode material YSZ-Ni [2,15–21]. For the purpose of this study the YSZ-Ni catalysed rate data is used. The rate data presented in the literature varies greatly due to the use of different material structures and different amounts of catalyst. For comparison, Fig. 7 shows the effect of temperature on the rate of hydrogen production for each chemical reaction ($S_{\text{s,H}_2}$ and $S_{\text{r,H}_2}$) using the data of Xu and Froment [15] and a curve fit to the data of Lehnert et al. [2]. The rates of hydrogen production presented here are calculated at the composition and pressure given in Table 2 and are normalised for ease of comparison. Fig. 7 shows that there is good qualitative agreement between the two data sets but significant quantitative differences at the higher temperatures.

Arrhenius curve fits to the data of Lehnert et al. [2,21] are used to describe both the catalysed shift reaction,

$$S_{\text{s,H}_2} = k_{\text{sf}}\left(p_{\text{H}_2\text{O}}p_{\text{CO}} - \frac{p_{\text{H}_2}p_{\text{CO}_2}}{K_{ps}}\right)\ (\text{mol}\,\text{m}^{-3}\,\text{s}^{-1}) \tag{30}$$

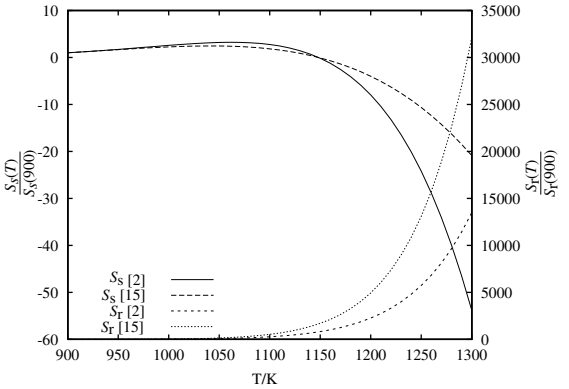

Fig. 7. Effect of temperature on the shift (s) and reforming (r) reaction rates. S is the mass rate of production (of H_2) per unit volume.

$$k_{sf} = 0.0171 \exp\left(-\frac{103\,191}{RT}\right) (\mathrm{mol\,m^{-3}\,Pa^{-2}\,s^{-1}}) \quad (31)$$

and the catalysed steam reforming of methane,

$$S_{r,H_2} = k_{sf}\left(p_{CH_4} p_{H_2O} - \frac{p_{H_2}^3 p_{CO}}{K_{pr}}\right) (\mathrm{mol\,m^{-3}\,s^{-1}}) \quad (32)$$

$$k_{rf} = 2395 \exp\left(-\frac{231\,266}{RT}\right) (\mathrm{mol\,m^{-3}\,Pa^{-2}\,s^{-1}}) \quad (33)$$

where R is the universal gas constant with units ($\mathrm{J\,mol^{-1}\,K^{-1}}$). The rate of production of each species due to each chemical reaction can be inferred from the rate equations (30), (32) and from the balanced chemical reactions (23) and (24).

4. The numerical scheme

4.1. General description

The conservation equations are solved using a finite volume time-marching method on a structured rectangular grid with variables stored at cell vertices, see Fig. 8. It should be noted that the numerical solution method is not currently time-accurate and time is used as a pseudo-variable simply to facilitate convergence to the steady-state solution. Variable grid spacing is used to create a finer grid near the domain boundaries to capture boundary layer effects. This code was based on a code originally developed for compressible turbomachinery calculations by Denton [22].

The discretized equations are solved at each computational grid cell to provide a new estimate of the primary variables in the centre of that cell. The calculation of the fluxes through the cell surfaces is straightforward because of the cell vertex storage scheme. All the first order derivatives calculated at internal cell vertices within the computational domain are evaluated using central differences. Those derivatives calculated at cell vertices on the external cell boundaries of the domain are calculated using one-sided differences.

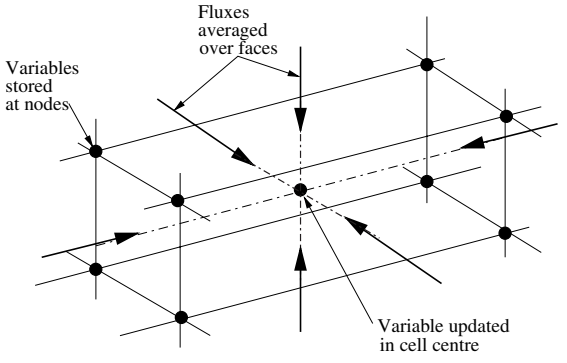

Fig. 8. Diagram showing a computational cell and the storage of information.

The time marching procedure begins with an initial guess based on the fuel channel inlet boundary conditions given in Table 2. These boundary properties are applied over the entire computational domain and are used to calculate the primary variables $(\rho_i, (\rho e)_{eff}, \mathbf{U}_p)$ at every cell vertex.

The solution procedure over one time step can be broken down into the following stages:

(1) At every cell vertex the physical properties of the gas mixture (p, T, μ, λ, X_i, D_{ij}) are calculated from the primary variables.
(2) Every five time steps $\mathbf{g}$, $\mathbf{q}_{eff}$ and S_i are updated at every cell vertex.
(3) The pore velocity at the cell centre is overwritten using a finite volume form of Eq. (8) given here in the x-direction,

$$(U_{px})_{cell} = \frac{K}{\varepsilon\mu V}\left[\int_{s_y} \mu \frac{\partial U_{px}}{\partial y}\mathrm{d}s_y + \int_{s_z} \mu \frac{\partial U_{px}}{\partial z}\mathrm{d}s_z - \int_{s_x} p\,\mathrm{d}s_x\right] \quad (34)$$

where V is the volume of the grid cell, s_x is the projection of the cell surface vector $\mathbf{s}$ onto a plane with a normal vector in the x-direction and similarly for s_y and s_z. The new estimate of velocity $(\mathbf{U}_p)_{cell}$ is calculated based on the current pressure field and the velocity gradients evaluated at the cell vertices from the previous time step. The cell-vertex values of velocity are then obtained by taking a mean of the cell-centred values surrounding each vertex.

(4) The change in species density $(\Delta\rho_i)_{cell}$ over a time step Δt is calculated using a finite volume form of Eq. (9),

$$(\Delta\rho_i)_{cell} = \frac{\Delta t}{V}\left[-\int_{\mathbf{s}} \rho_i \mathbf{U}_{pi}\cdot\mathrm{d}\mathbf{s} + S_i V\right] \quad (35)$$

The density changes $(\Delta\rho_i)_{cell}$ are distributed to the densities stored at the cell vertices ρ_i using a similar process as above.

(5) The change in the specific energy at the centre of each grid cell $(\Delta(\rho e)_{eff})_{cell}$ is calculated similarly,

$$(\Delta(\rho e)_{eff})_{cell} = \frac{\Delta t}{V}\left[-\int_{\mathbf{s}} \left(\rho_g h_g \varepsilon \mathbf{U}_p + \mathbf{q}_{eff} + \sum_{i=1}^{n} \frac{\varepsilon \mathbf{g}_i}{\beta} h_i\right)\cdot\mathrm{d}\mathbf{s}\right] \quad (36)$$

The energy changes $(\Delta(\rho e)_{eff})_{cell}$ are then distributed to the energy stored at the cell vertices $(\rho e)_{eff}$ in the same way.

This process is repeated over many time steps until the converged steady-state solution is found. This numerical scheme requires no artificial dissipation or smoothing and the converged solution is therefore second-order accurate.

4.2. Physical properties

In step (1) the physical properties of the gaseous mixture are evaluated. The temperature of the gas T is obtained by solving Eqs. (17)–(21). The pressure p is calculated from the ideal gas equation

$$p = \rho_g \frac{R}{\widetilde{M}} T \tag{37}$$

where the mean molar mass $\widetilde{M}$ is calculated locally from the current gas composition. The values of gas viscosity and thermal conductivity are functions of temperature and composition. For each species, the variation of each property with temperature is defined by a quadratic curve fit to tabulated data [23]. A mole fraction average

$$\mu_g = \sum_{i=1}^{n} X_i \mu_i \tag{38}$$

is used to obtain an estimate of the properties at a given gas composition. Although this method is not the most accurate available it is computationally cheaper than the methods of Reichenberg and Wassiljewa [23] and was shown to give acceptable accuracy over the range of interest.

4.3. Boundary conditions

4.3.1. Solid walls

At the solid walls, the prescribed boundary values are used to overwrite the variables computed by the numerical procedure. The fluxes normal to the solid walls are set as in Table 2. The mass-averaged velocity is set in conjunction with the diffusion velocity to give the correct flux of each species, see Eq. (10). A no-slip boundary condition is applied to the tangential flow along the solid walls, see Fig. 9. This affects the velocity gradient at the wall and allows a boundary layer to form.

4.3.2. Interface boundary

At an interface boundary it is necessary to set the values of properties rather than fluxes. If it could be assumed that the adjoining gas represented a stationary infinite source or sink, the properties would be constant over the boundary. However, in this study, the gas in the fuel channel is not stationary. The variation of gas properties along the fuel channel are estimated from a one-dimensional enthalpy and mass balance, see Fig. 10. Conduction, diffusion and chemical reaction in the fuel channel are currently ignored, although the intention is, eventually, to include the fuel channel in the calculation scheme.

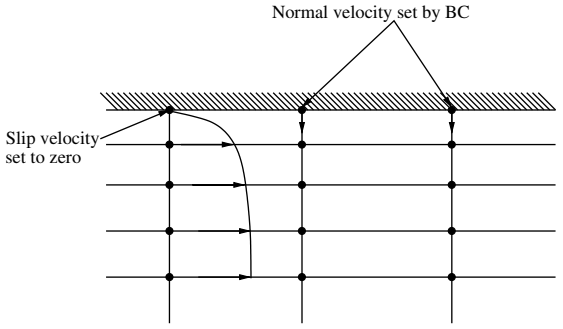

Fig. 9. Boundary conditions at a solid wall.

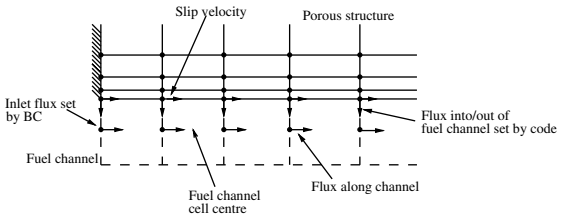

Fig. 10. Boundary conditions at the interface between the porous structure and the fuel channel.

The properties at the fuel channel inlet are specified in Table 2. The properties along the channel are updated using a similar time-marching method to the main numerical scheme:

(1) Calculate the mean velocity at each axial position based on the axial pressure gradient, a friction factor and the wall slip velocity predicted by the code.
(2) Estimate the fluxes along the channel at each axial position.
(3) Sum the fluxes along the fuel channel and through the porous wall to give the net influx into each fuel channel cell.
(4) Multiply the net influx by a time step to give the change in properties at the centre of each cell.
(5) Distribute the changes to the vertices at the porous boundary.
(6) Apply the velocity gradient normal to the surface of the porous wall as a boundary condition on the porous domain, see Eq. (A.7) in the Appendix A.

4.4. Time step

In order to speed convergence to the steady-state solution a multi-grid method is employed whereby the flow property changes at each time step are summed on

three separate computational grids. The three grids vary in size from a grid that represents the entire computational domain with one large cell to a grid where each cell is represented individually. This results in non-time-accurate marching toward a steady-state solution because changes can be convected through the computational domain at a much higher speed than using a single grid. The allowable time step is estimated using the overall conservation of mass equation

$$\frac{\partial \rho_g}{\partial t} + \nabla \cdot (\rho_g \mathbf{U}_p) = 0 \tag{39}$$

which can be rewritten assuming $\rho_g = p/RT$, substituting for $\mathbf{U}_p$ from Eq. (6) and ignoring temperature variation to give

$$\frac{\partial p}{\partial t} = \frac{pK}{\mu_g \varepsilon} \nabla^2 p \tag{40}$$

Eq. (40) is an unsteady diffusion equation for pressure. The stability criterion for the one-dimensional version of this equation is

$$\frac{pK\Delta t}{\mu_g \varepsilon \Delta x^2} \leqslant \frac{1}{2} \tag{41}$$

The limiting value of Δt calculated from Eq. (41) can also be successfully applied to the three-dimensional simulation.

5. Results

The results presented below are calculated with the boundary conditions and physical properties given in Section 2. These properties and boundary conditions are representative of an IP-SOFC porous support and do not describe any particular experimental test case. In a real fuel cell stack containing thousands of IP-SOFC modules, the performance of any individual module will depend crucially on its interaction with the surrounding elements of the stack. Accurate and realistic specification of the boundary conditions, particularly those describing the thermal interaction, is therefore all important. The results presented below are therefore included for illustrative purposes to show the potential of the method.

The computational grid comprised 100 cells in the x-direction, 28 cells in the y-direction and 4 cells in the z-direction. The results are plotted on a cross-section through the computational domain as shown in Fig. 4. This cross-section is in the x–y plane, located at $z = L_z/2$. However, because of the boundary conditions adopted, no variation of the flow-field is expected to occur in the z-direction. The calculation took 16 h of computational time to converge on a 1.5 GHz Pentium 4 PC. It should be noted that a particularly low fuel channel mass flow rate was chosen to accentuate the variation of flow properties in the porous structure.

Fig. 11 shows the component of the gas velocity vector $\mathbf{U}_p$ in the x–y plane. The variation of the y-direction velocity U_{py} is shown in Fig. 12. A net mass flux enters the porous structure at the anode interface ($y = L_y$) and travels through the domain spreading by a small amount in the x-direction. The x-direction velocity U_{px} is shown in Fig. 13. Large variations of U_{px} are visible at the edges of each anode ($y = L_y$) where the flow spreads in the x-direction. Within the boundary layer adjacent to the fuel channel, U_{px} is of a similar magnitude as the variations at $y = L_y$. Fig. 14 shows the pressure distribution within the domain. The overall pressure gradient in the x-direction is caused by the prescribed pressure drop in the fuel channel. In order to conserve mass, the pressure increases in the regions adjacent to each anode where mass enters the system.

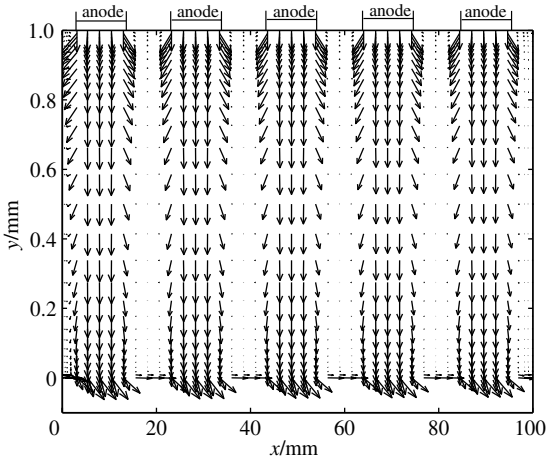

Fig. 11. Velocity vector distribution.

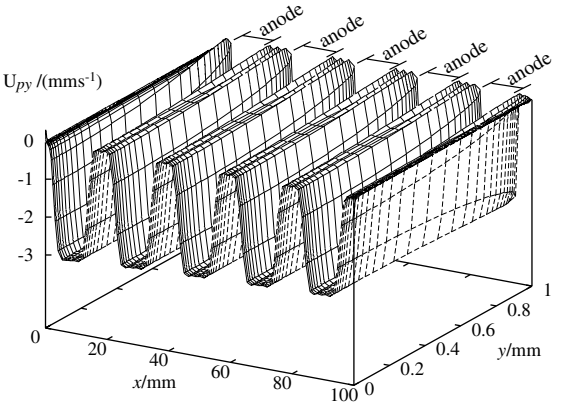

Fig. 12. y-direction velocity distribution.

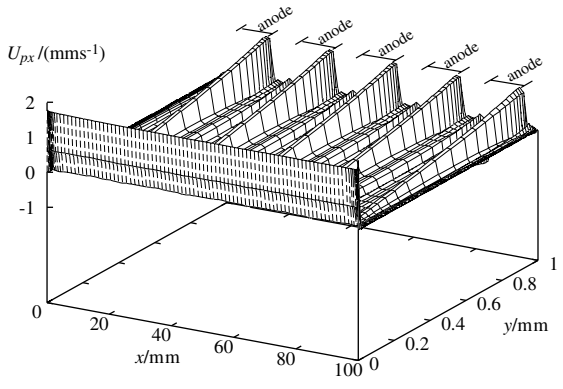

Fig. 13. x-direction velocity distribution.

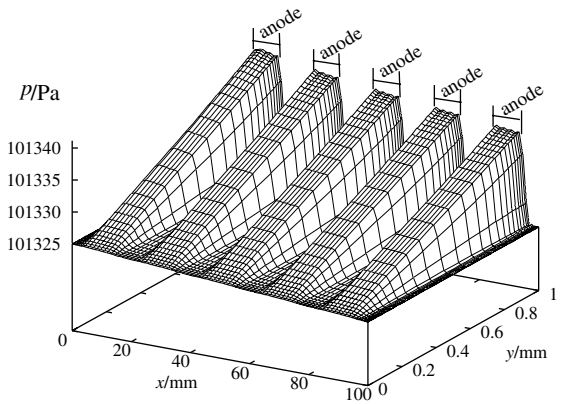

Fig. 14. Pressure distribution within the porous structure.

This pressure rise results in a pressure gradient in the x-direction which causes the spreading of the flow in the x-direction at the anode edges.

The temperature distribution, see Fig. 15, shows a decrease in the x-direction from the fuel channel inlet ($x = 0$). The temperature drop is caused by the endothermic methane reforming reaction which proceeds very quickly at the channel inlet where the temperature and the methane mole fraction are both high. Fig. 16 shows the rate of production of hydrogen as a result of this reaction. As the temperature drops, the methane reforming reaction rate decreases (see Fig. 7) and the heat input at each anode (from the electrochemical reactions) causes the x-direction temperature gradient to increase gradually. The distribution of the methane mole fraction, see Fig. 17, confirms that the reduction in the rate of hydrogen production is not due to the consumption of the methane present but is a result of the temperature dependency of the reforming reaction rate.

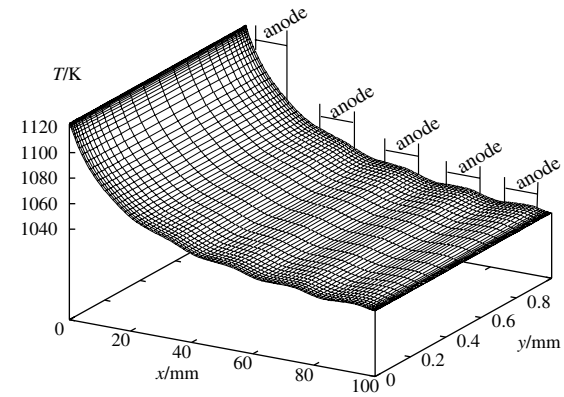

Fig. 15. Temperature distribution within the porous structure.

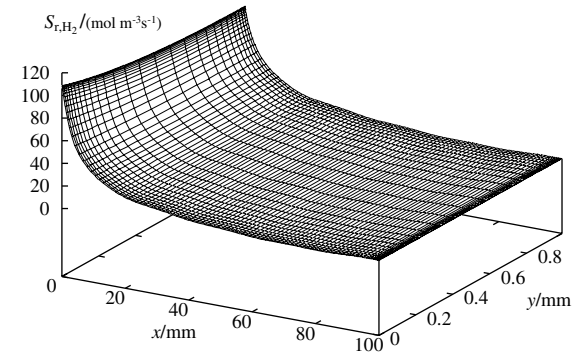

Fig. 16. Rate of hydrogen production due to the methane reforming reaction.

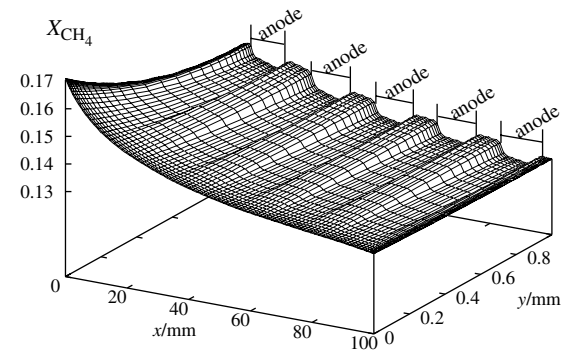

Fig. 17. Methane mole fraction distribution within the porous structure.

As shown in Fig. 18, the mole fraction of hydrogen X_{H_2} is locally low at the anode surfaces where it is consumed. However, in between the anodes X_{H_2} increases as a result of the chemical reactions. At the fuel

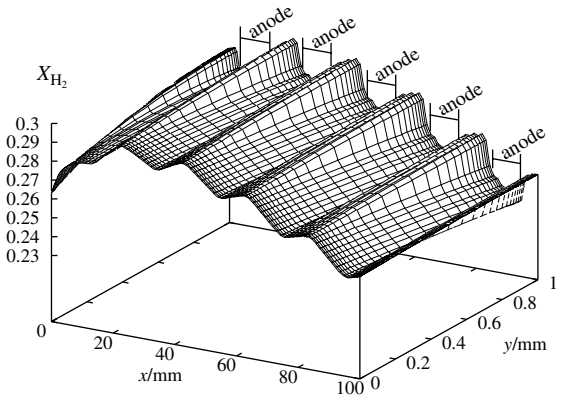

Fig. 18. Hydrogen mole fraction distribution within the porous structure.

channel inlet there is a net increase in X_{H_2} as more hydrogen is produced by the methane reforming reaction than is consumed at the anodes. As S_{r,H_2} decreases with increasing x, the opposite behaviour is observed and there is a net decrease in X_{H_2} as more hydrogen is consumed at the anodes than is produced by the chemical reactions. Similarly, Fig. 19 shows that there is a net increase in X_{H_2O} toward the end of the fuel channel. The rate of hydrogen production by the shift reaction, see Fig. 20, increases at the anode surfaces where conditions are favourable due to the low value of X_{H_2} and the high value of X_{H_2O}.

Finally, it should be noted that the calculations were performed assuming a constant heat flux into the domain from the anodes. In practice the fall in temperature in the x-direction would result in reduced voltage and heat production in successive electrochemical cells. The accurate representation of such effects clearly requires more detailed modelling of the cell electrochemistry.

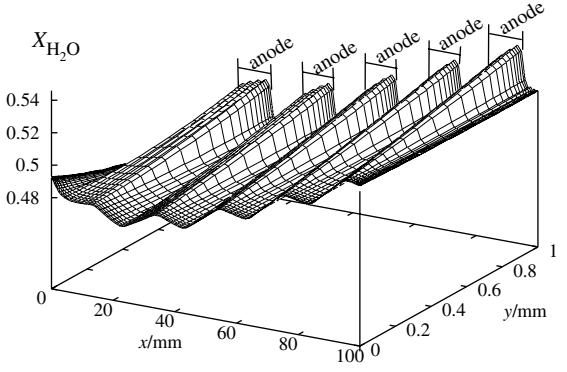

Fig. 19. Steam mole fraction distribution within the porous structure.

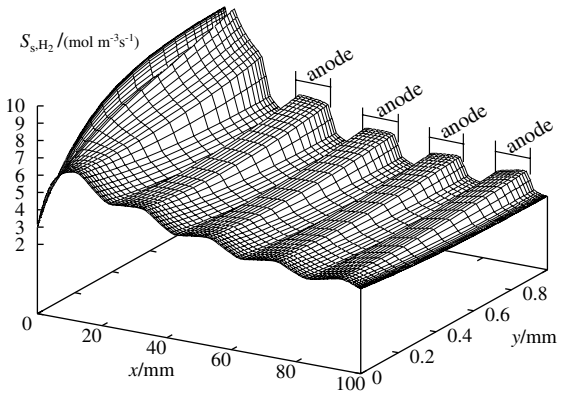

Fig. 20. Rate of hydrogen production due to the shift reaction.

6. Conclusions

A method for solving the multi-component steady-state gas flow with chemical reaction in the porous support structure of an IP-SOFC has been demonstrated. The method is fully three-dimensional and provides detailed information on the flow field which cannot be obtained by simpler, more approximate models. Multi-component diffusion is handled correctly by solving the Stefan–Maxwell equations and an arbitrary number of gas components can be included. The catalysed shift and methane reforming reaction rates are also modelled, the local temperature being obtained by solving the complete energy equation including heat conduction in the gas and solid, and enthalpy transport by convection and diffusion. Another novel feature of the method is its ability to compute the velocity boundary layers at the edges of the porous structure. This is particularly important at the interface with the fuel channel.

A sample calculation has been used to illustrate the potential of the method. Although this was not related to a particular experimental situation, it has demonstrated the importance of the temperature dependence of the methane reforming reaction. More realistic results would require the careful matching of the boundary conditions to the exact physical situation together with improved modelling of the fuel cell electrochemistry and the fuel channel fluid mechanics. Work along these lines is currently in progress at Cambridge.

Acknowledgements

B.A.H was supported by an EPSRC research studentship and a Rolls-Royce CASE award. The authors are indebted to Prof. J.D. Denton of the Whittle laboratory, University of Cambridge for generously making available his time-marching computer program for

turbomachinery flows. They are also grateful for the technical assistance supplied by the staff of Rolls-Royce Fuel Cell Systems Ltd., particularly Dr. G. Agnew, Mr. R. Collins and to Mr B. Todd of the Cambridge University Engineering Department.

Appendix A. Estimation of boundary layer size

There are two types of boundary layers that can form within a porous material. The first is due to flow over a solid surface. The equation governing a fully-developed flow through a plane, two-dimensional porous channel with solid walls is

$$\frac{\partial p}{\partial x} = \mu_g \frac{\partial^2 U_{px}}{\partial y^2} - \frac{\mu_g \varepsilon}{K} U_{px} \tag{A.1}$$

Assuming $y = 0$ at the channel centre-line and a channel half-width of y_d, the boundary conditions are

$$U_{px}(y_d) = 0, \quad \left.\frac{\partial U_{px}}{\partial y}\right|_{y=0} = 0 \tag{A.2}$$

The solution is

$$U_{px}(y) = \frac{\partial p}{\partial x}\frac{K}{\mu_g \varepsilon}\left(\frac{\cosh\left(y\sqrt{\frac{\varepsilon}{K}}\right)}{\cosh\left(y_d\sqrt{\frac{\varepsilon}{K}}\right)} - 1\right) \tag{A.3}$$

The boundary layer thickness δ_H is defined as the distance from the wall where the velocity U_{px} is equal to 99% of the velocity defined by the unmodified Darcy Equation (6). This is equal to

$$\delta_H = y_d - \sqrt{\frac{K}{\varepsilon}}\ln\left[0.02\cosh\left(y_d\sqrt{\frac{\varepsilon}{K}}\right)\right] \tag{A.4}$$

which for the parameters in this study, reduces to

$$\delta_H \approx -\sqrt{\frac{K}{\varepsilon}}\ln 0.02 \approx 0.01 \text{ mm} \tag{A.5}$$

and represents 1% of L_y. This result agrees well with the work of Vafai and Tien [24] on high porosity foam metals.

A boundary layer can also be formed at the interface between the porous domain and the fuel channel. Beavers and Joseph [25] introduced the concept of an interface velocity, $U_{x,\text{int}}$, which results from the need to match the velocity gradient as well as the velocity at the interface of the gaseous and porous flow, see Fig. 21.

The flows in the fuel channel and in the porous structure are both induced by the same pressure gradient. It is possible to estimate the size of the boundary layer in the porous structure from the equations for fully-developed porous and non-porous flow, Eq. (A.1) and

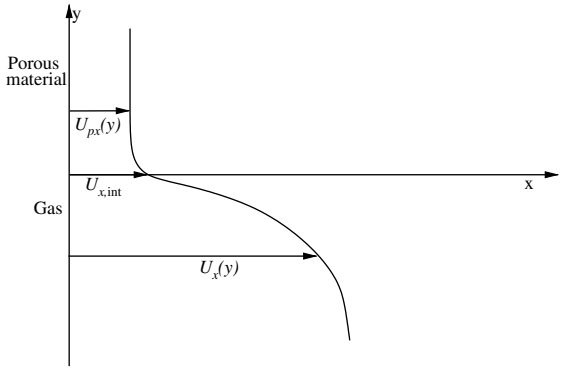

Fig. 21. Sketch of the velocity distribution near the interface between the porous structure and the fuel gas channel.

$$\frac{\partial p}{\partial x} = \mu_g \frac{\partial^2 U_x}{\partial y^2} \tag{A.6}$$

respectively where U_x is the velocity in the gas channel. The velocity gradient for a fully-developed flow in a gas channel of width $2y_c$ with slip is independent of the slip velocity and is obtained from Eq. (A.6) as

$$\frac{\partial U_x}{\partial y} = \frac{1}{\mu_g}\frac{\partial p}{\partial x} y \tag{A.7}$$

This velocity gradient, evaluated at the channel wall ($y = y_c$) is used as a boundary condition to solve Eq. (A.1) to give

$$U_{px}(y) = -\frac{K}{\varepsilon\mu_g}\frac{\partial p}{\partial x}\left[\frac{\sinh\left(y\sqrt{\frac{\varepsilon}{K}}\right)}{\cosh\left(y_d\sqrt{\frac{\varepsilon}{K}}\right)} y_c\sqrt{\frac{\varepsilon}{K}} + 1\right] \tag{A.8}$$

The interface velocity, $U_{x,\text{int}}$, is given by $U_{px}(y_d)$ as

$$U_{x,\text{int}} = U_{px}(y_d) = -\frac{K}{\varepsilon\mu_g}\frac{\partial p}{\partial x}\left[y_c\sqrt{\frac{\varepsilon}{K}} + 1\right] \approx 4.5 \text{ mm s}^{-1} \tag{A.9}$$

The boundary layer thickness is calculated as the distance from the interface to where the velocity = 101% of the Darcian velocity. For the parameters in this study the boundary layer thickness is therefore given by

$$\delta_H = -\sqrt{\frac{K}{\varepsilon}}\ln\left[\frac{0.02}{y_c\sqrt{\frac{\varepsilon}{K}}}\right] \approx 0.025 \text{ mm} \tag{A.10}$$

which represents 2.5% of L_y. Fig. 22 shows the analytical solutions for the interface boundary layer velocity profile for different values of permeability. A comparison is also made with the velocity profiles calculated using the numerical method described in this paper.

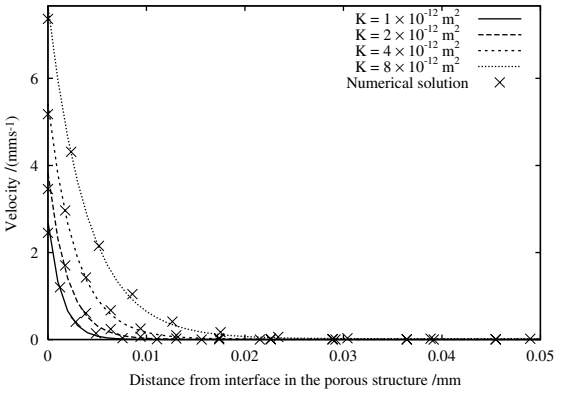

Fig. 22. Analytical solution for the velocity boundary layers in the porous structure adjacent to the fuel channel, see Eq. (A.8). The equivalent numerical solutions, using the method described in this paper, are plotted for comparison.

References

[1] F.J. Gardner, M.J. Day, M.P. Brandon, M.N. Pashley, M. Cassidy, SOFC technology development at Rolls-Royce, J. Power Sources 86 (2000) 122–129.

[2] W. Lehnert, J. Meusinger, F. Thorn, Modelling of gas transport phenomena in SOFC anodes, J. Power Sources 87 (2000) 57–63.

[3] T. Ackmann, L.G.J. Haart, W. Lehnert, D. Stolten, Modelling of mass and heat transport in planar substrate type SOFCs, J. Electrochem. Soc. 150 (2003) 783–789.

[4] J. Yuan, M. Rokni, B. Sunden, Three-dimensional computational analysis of gas and heat transport phenomena in ducts relevant for anode-supported solid oxide fuel cells, Int. J. Heat Mass Transfer 46 (2003) 809–821.

[5] H.C. Tien, K.C. Chiang, Non-Darcy flow and heat transfer in a porous insulation with infiltration and natural convection, J. Marine Sci. Technol. 7 (1999) 125–131.

[6] P.X. Jiang, Z.P. Ren, Numerical investigation of forced convection heat transfer in a porous media using a thermal non equilibrium model, Int. J. Heat Fluid Flow 22 (2001) 102–110.

[7] D.R. Marpu, Forchheimer and Brinkman extended Darcy flow model on natural convection in a vertical cylindrical porous annulus, Acta Mech. 109 (1995) 41–48.

[8] C.T. Hsu, P. Cheng, The Brinkman model for the natural convection about a semi-infinite vertical plate in a porous medium, Int. J. Heat Mass Transfer 28 (1985) 683–697.

[9] B. Todd, Mass transport in solid oxide fuel cell electrodes, in: 2nd International Conference on Heat Transfer, Fluid Mechanics and Thermodynamics, number TB1, Victoria Falls, Zambia, 2003.

[10] M. Kaviany, Laminar flow through a porous channel bounded by isothermal parallel plates, Int. J. Heat Mass Transfer 28 (1985) 851–858.

[11] M.V. Twigg (Ed.), Catalyst Handbook, Wolfe Pub. Ltd., 1989.

[12] F. Bustamante, R. Enick, K. Rothenberger, B. Howard, A. Cugini, M. Ciocco, B. Morreale, Kinetic study of the reverse water gas shift reaction in high- temperature, high pressure homogeneous systems, Fuel Chem. Div. Preprints 47 (2002).

[13] V.F. Kochubei, F.B. Moin, Kinetics of the reaction of CO_2 with hydrogen, Kinetika i Kataliz 10 (1969) 1203–1209.

[14] G.L. Tingey, Kinetics of the water–gas equilibrium reaction. 1. the reaction of carbon dioxide with hydrogen, J. Phys. Chem. 70 (1966) 1406–1412.

[15] J. Xu, G.F. Froment, Methane steam reforming, methanation and water gas shift: 1. Intrinsic kinetics, AIChE J. 35 (1989) 88–96.

[16] E. Achenbach, Riensche, Methane/steam reforming kinetics for solid oxide fuel cells, J. Power Sources 52 (1994) 283–288.

[17] R. Peters, R. Dahl, U. Kluttgen, C. Palm, D. Stolten, Internal reforming of methane in solid oxide fuel cell systems, J. Power Sources 106 (2002) 238–244.

[18] A.L. Dicks, K.D. Pointon, A. Siddle, Intrinsic reaction kinetics of methane reforming on a Nickel/Zirconia anode, J. Power Sources 86 (2000) 523–530.

[19] S.H. Clarke, A.L. Dicks, K. Pointon, T.A. Smith, A. Swann, Catalytic aspects of the steam reforming of hydrocarbons in internal reforming fuel cells, Catal. Today 38 (1997) 411–423.

[20] J. Meusinger, E. Riensche, J. Stimming, Reforming of natural gas in solid oxide fuel cell systems, J. Power Sources 71 (1998) 315–320.

[21] I. Drescher, W. Lehnert, J. Meusinger, Structural properties of SOFC anodes and reactivity, Acta Electrochim. 43 (1998) 3059–3068.

[22] J.D. Denton, The calculation of three-dimensional viscous flow through multistage turbomachines, ASME J. Turbomach. 114 (1992) 18–26.

[23] B. Todd, J.B. Young, Thermodynamic and transport properties of gases for use in solid oxide fuel cell modelling, J. Power Sources 110 (2002) 186–200.

[24] K. Vafai, C.L. Tien, Boundary and inertia effects on flow and heat transfer in porous media, Int. J. Heat Mass Transfer 24 (1981) 195–203.

[25] S.G. Beavers, D.D. Joseph, Boundary conditions at a naturally permeable wall, J. Fluid Mech. 30 (1967) 197–207.